J MATER SCI **41** (2006) 611–619

Morphology and interfacial structure of gamma precipitates in the beta phase of a Ti-Al-Nb-Zr alloy

L. C. ZHANG, M. AINDOW*
Department of Materials Science and Engineering, Institute of Materials Science, University of Connecticut, Storrs, CT 06269-3136, USA
E-mail: m.aindow@uconn.edu

The morphology and interfacial structure of γ precipitates in the β phase of a Ti-44%Al-4%Nb-4%Zr alloy have been studied using transmission electron microscopy. The γ precipitates exhibit an acicular morphology bounded by two principal facets and two minor facets. One of the major facets adopts a commensurate singular interface structure, which forms at an orientation close to the Kurdjumov-Sachs relationship. On an atomic scale these facets adopt a 'step-terrace' configuration, and the coherency strain on the terrace is relieved by the dislocation character of the steps. The other major facet adopts a one-dimensionally incommensurate singular interface structure at the Pitsch orientation relationship. The angular incompatibility between these two singular structures is accommodated by dislocations in the incommensurate interface. The configuration of these dislocations suggests that this is accomplished by nucleation at the facet junctions and subsequent climb along the facets.

1. Introduction

Alloys based on aluminides of titanium have been the subject of intensive research in the metallurgical community for several decades. The primary motivation for this activity has been the development of materials for high-temperature structural applications, because titanium aluminides offer an attractive combination of low density and good high-temperature properties. The emphasis in most recent work has been upon alloys which contain 45–50 atomic % Al and exhibit a lamellar mixture of $L1_0$ γ-TiAl and $D0_{19}$ α_2-Ti_3Al phases. The strength and creep resistance of such alloys can be improved further by the addition of transition metals such Nb, Zr, Ta and Hf, which tend to stabilize the high-temperature BCC β phase [1, 2]. When alloys containing these elements are cooled from the $\alpha + \beta$ phase field, however, there is a wide range of different microstructures which can arise. For example, Cheng and Loretto analyzed the transformed β microstructures in alloys containing 44 at% Al and 8 at% (Nb + Zr): it was found that the morphology of the transformation products was very sensitive to cooling rate [3]. One of the more interesting phenomena observed was the formation of acicular γ precipitates within the β phase implying that there must be a three-phase $\alpha + \beta + \gamma$ phase field directly below the $\alpha+\beta$ phase field in which the alloys are heat-treated.

In this paper we present a transmission electron microscopy (TEM) study of the γ precipitates in the β phase of one of these alloys. High-resolution TEM (HRTEM) lattice imaging has been used to reveal the structure and defect content of facets on the precipitate-matrix interfaces. It is shown that the structures of the two major facets are related to well-defined singular configurations but that these occur at *different* orientation relationships. The accommodation of this angular incompatibility is analyzed and compared with that observed recently for crystallographically similar precipitates in a duplex stainless steel [4]. The consequences of these observations for the nucleation and growth of these precipitates is discussed.

2. Experimental procedure

The TEM investigations were performed on samples from an alloy with a composition of Ti-44Al-4Nb-4Zr-0.2Si-0.3B (atomic %). The alloy was prepared as a 0.8 kg button using transferred-arc plasma melting under argon in a water-cooled copper hearth. The button was remelted 5 times to ensure chemical homogeneity. Following casting,

*Author to whom all correspondence should be addressed.
0022-2461
DOI: 10.1007/s10853-006-6477-z

the material was hot-isostatically-pressed at 1250°C for 4 hours at 150 MPa to reduce porosity and microcracking. This was then forged isothermally at 1150°C to a 70% reduction in height at a strain rate of 5×10^{-3} s^{-1} to break up the as-cast structure. The forged material was heat-treated at 1350°C for 1 h followed by water-quenching.

TEM specimens were prepared by twin-electropolishing to perforation using an electrolyte consisting of 6% perchloric acid, 34% butan-1–o1, and 60% methanol at −15°C followed by Ar+ ion milling briefly at low voltage (1–3 kV) to remove any residual contamination on the sample surfaces. Conventional TEM data were obtained in a Philips EM420 operating at 100 kV, whereas HRTEM images were obtained in a JEOL 2010 FasTEM equipped with an EDAX Phoenix energy-dispersive X-ray spectrometer (EDXS) and operating at 200 kV. The objective lens on this latter instrument has a spherical aberration coefficient of 0.5 mm giving a point-to-point resolution of <0.19 nm at Scherzer defocus. The defect character of interfacial features observed in the HRTEM images was analyzed using the topological theory of interfacial defects [5, 6] and the associated circuit mapping procedures [7].

3. Results

3.1. Overall microstructure

Fig. 1a is an SEM image showing the overall microstructure exhibited by the alloy. This consists of large equi-axed grains of the α_2 phase, up to 100 μm in diameter, with regions of other phases along the grain boundaries and at the triple lines. As described previously [3], these regions exhibit mainly the bcc β phase with extensive B2 and/or ω ordering, and precipitates of the γ phase are usually contained within these regions. One such region is shown in Fig. 1b. The γ precipitates are acicular with lengths of up to 10 μm and an aspect ratio of 10–30. Chemical microanalysis using EDXS revealed that the composition of these γ precipitates is different from that of the surrounding β phase and mean values for the measured compositions are given in Table I.

The OR of the γ precipitates with respect to the surrounding matrix was determined using selected area electron diffraction (SAED) patterns. One example is shown in Fig. 1c, which was obtained with the beam direction parallel to the major axis of one of the precipitates. In each case the orientation was found to be close to the Kurdjumov-Sachs (K-S) OR, i.e.:

$$\{1\,1\,1\}_\gamma // \{1\,0\,\bar{1}\}_\beta$$
$$\langle 1\,\bar{1}\,0\rangle_\gamma // \langle 1\,1\,1\rangle_\beta$$

More detailed measurements using convergent beam Kikuchi patterns revealed a small deviation from the K-S OR. The sense and magnitude of this deviation was consistent from particle-to-particle and this corresponded to a rotation away from the Pitsch OR:

$$\{0\,0\,\bar{1}\}_\gamma // \{0\,\bar{1}\,1\}_\beta$$
$$\langle 1\,\bar{1}\,0\rangle_\gamma // \langle 1\,1\,1\rangle_\beta$$

The magnitude of the measured rotation was 0.5°.

The details of the particle morphology were determined by comparing diffraction contrast TEM images with SAED patterns. The major axis of each precipitate was close to the conjugate close-packed directions ($[\bar{1}\bar{1}\bar{1}]_\beta$ and $[\bar{1}10]_\gamma$). Although the cross-sections of these γ precipitates varied somewhat from particle to particle, all were faceted. Fig. 1d is a schematic diagram showing the four distinct facets observed by TEM. As explained in the following sections, two of these are coherent (designated C_1 and C_2) whereas the other two (designated I_1 and I_2) are partially incoherent. The two major facets, which can be up to 500 nm wide, are C_1 approximately parallel to $(112)_\gamma/(21\bar{3})_\beta$, and I_1 approximately parallel to $(110)_\gamma/(2\bar{1}\bar{1})_\beta$. In many cases, narrower (<20 nm wide) segments of facets C_2, approximately parallel to $(111)_\gamma/(10\bar{1})_\beta$ and I_2, which lies parallel to $(001)_\gamma$, were also observed.

TABLE I Mean compositions (in atomic %) of the three phases present in the alloy after heat-treating at 1350°C, as measured using EDXS

	Ti	Al	Nb	Zr	Si
α_2	43.7	43.1	5.9	6.0	1.4
β	50.6	34.6	6.9	6.9	1.0
γ	38.9	46.5	6.1	6.6	2.0

3.2. HRTEM observation of various facets and facet junctions

Since all four of the facets contain the conjugate close-packed directions, these interfaces are oriented edge-on in images obtained at this zone axis. As such, the crystallography of this system is particularly convenient for HRTEM studies. Examples of the HRTEM data obtained from each of the facets, and the junctions between them, are presented in this section. More detailed analyses of the defect content in the C_1 and I_1 facets are presented in Sections 3.3 and 3.4, respectively.

Representative HRTEM images obtained from regions of the four facets are shown in Fig. 2. The structure of the C_1 facet is shown in Fig. 2a. Although the average interface orientation is approximately $(112)_\gamma//(21\bar{3})_\beta$, it is clear from such micrographs that the interface is corrugated on an atomic scale. This facet may be described more accurately as adopting a 'step-terrace' configuration: the terraces lie parallel to $(111)_\gamma//(10\bar{1})_\beta$, and these are separated by steps a single inter-planar spacing in

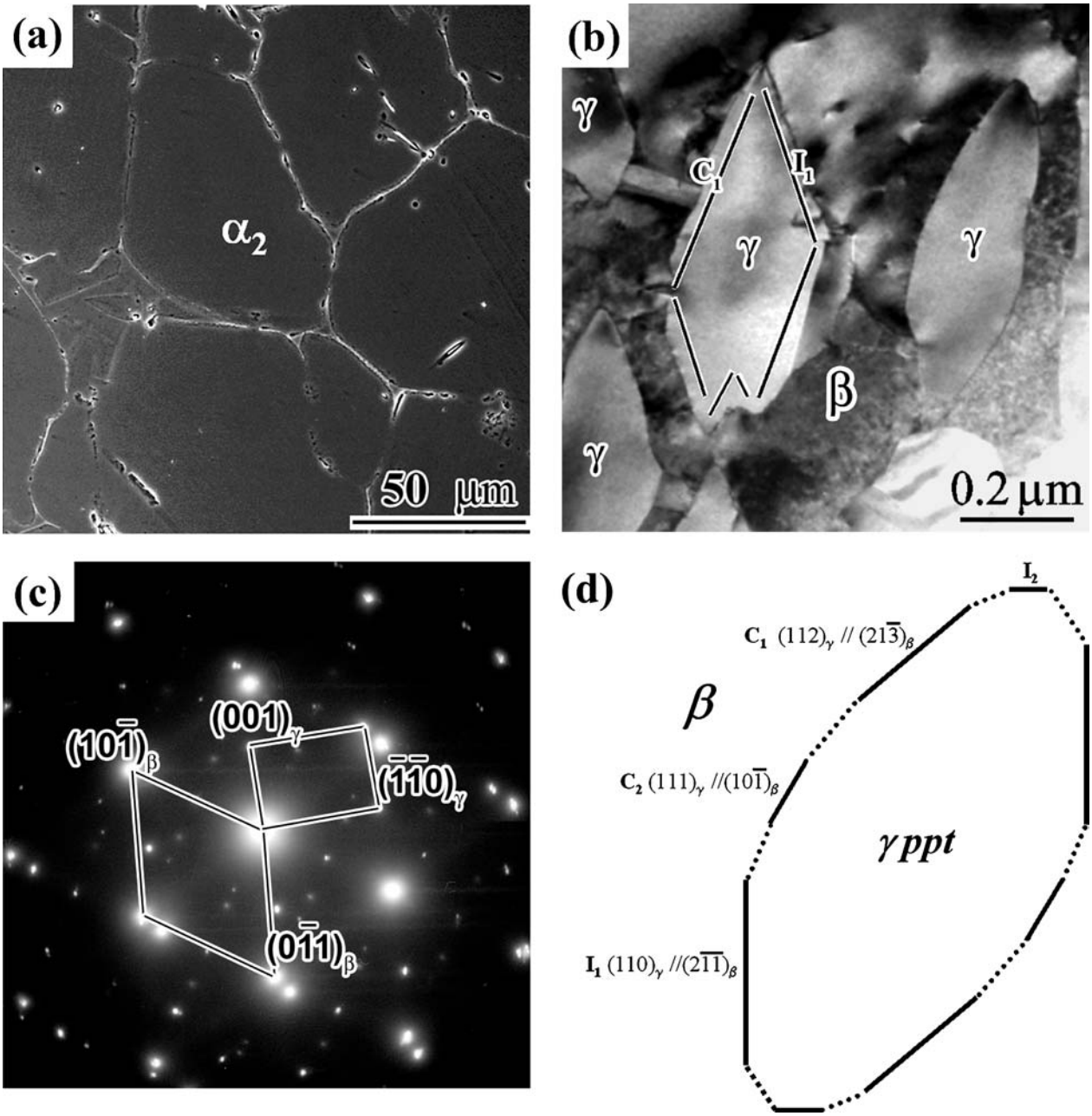

Figure 1 Key microstructural features of the alloy: (a) secondary electron SEM image showing the main α_2-phase with β phase regions at the boundaries and triple lines; (b) bright-field TEM micrograph showing the faceted cross-section of γ precipitates within the β phase; (c) SADP showing the near-K-S OR for the precipitates; (d) schematic diagram showing the relative orientation/position of the various facets and the junctions between them.

height ($h = 0.2486$ nm). The average spacing of these steps (i.e. the terrace width), d, measured parallel to the habit plane is ≈ 0.7 nm which corresponds closely to the angular deviation of $\tan^{-1}(h/d) \approx 19^\circ$ between the terrace and habit planes. We note that the average step spacing did not vary from area to area on a given C_1 facet, from one C_1 facet to another on a given particle, or from particle to particle, implying that this corresponds to a particularly favorable configuration for these facets. Fig. 2b shows the structure for a small region of the C_2 facet. In contrast to the C_1 facet, these minor facets are atomically flat with $(111)_\gamma//(10\bar{1})_\beta$. Thus, the structure of the C_2 facet corresponds to that of the terraces on the C_1 facets. Both of these facets show a one to one correspondence of lattice sites across the interface with no isolated crystal dislocations or other lattice defects: as such, they were designated coherent (C) facets. No such lattice registry was observed for the I_1 and I_2 facets shown in Fig. 2c and d, respectively. As such, these were designated incoherent (I) facets although it is important to recall that the coherence along the beam direction will be the same as for the C facets. Both of the I facets are atomically flat with

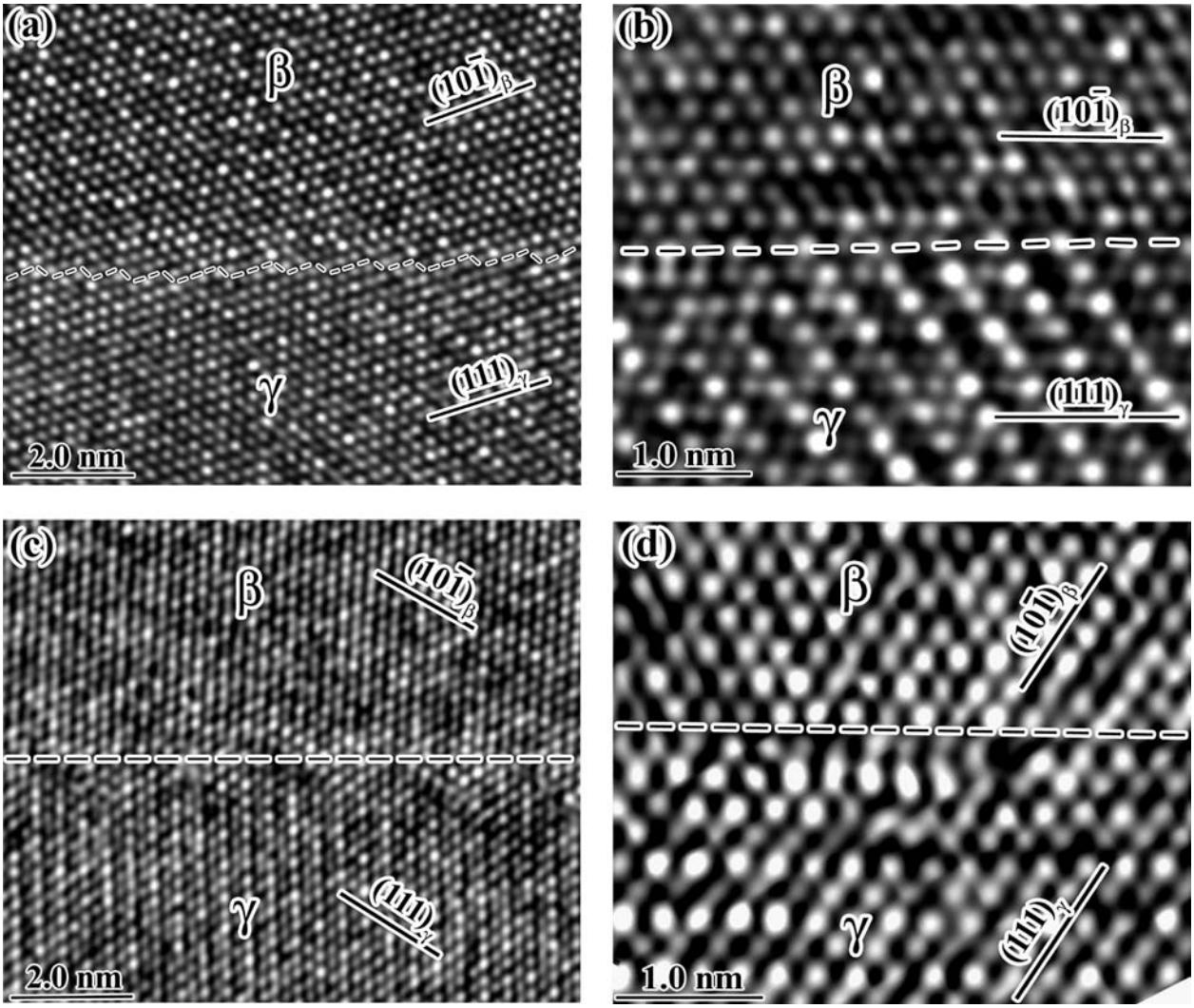

Figure 2 HRTEM images obtained with $\mathbf{B} = [\bar{1}\bar{1}\bar{1}]_\beta * // [\bar{1}10]_\gamma *$ showing: (a) a coherent C_1 facet approximately parallel to $(112)_\gamma$; (b) a coherent C_2 facet parallel to $(111)_\gamma$; (c) an incoherent I_1 facet parallel to $(110)_\gamma$; (d) an incoherent I_2 facet parallel to $(001)_\gamma$.

the major I_1 facets lying parallel to $(110)_\gamma/(2\bar{1}\bar{1})_\beta$ and the narrow I_2 facets lying parallel to $(001)_\gamma$. We note that the orientation of the I_2 facet corresponds to that of the risers on the steps on the C_1 facets. Isolated dislocations were observed in both the I_1 and the I_2 facets, and the character of these is discussed in detail in Section 3.4.

Although a wide variety of different particle cross-sections was observed, all of the interfaces corresponded to the four facets structures identified above, or combinations of these. Examples of HRTEM images obtained from such mixed regions are shown in Fig. 3a–d. An example of the structure observed at a C_1/C_2 facet junction is shown in Fig. 3a. This includes not only regions of C_1 and C_2 facets, but also small segments of I_2 facets. Similarly, Fig. 3b shows a region of C_2 facet interspersed with short segments of I_1 and I_2 facets. Simpler structures were observed at other facet junctions: Figs 3c and d were obtained from an I_1/C_2 and an I_2/I_1 junction respectively. In both cases the junction structure simply corresponds to a mixture of regions with the two corresponding facet structures. Thus, junctions that appear to be curved on a microscopic scale are facetted on an atomic scale and correspond to a gradual transition from one facet type to the next.

3.3. Structure and defect content of the C_1 facets

The origins of the corrugated structure adopted by the C_1 facets was revealed by comparing the results of circuit mapping procedures to the defect character expected on the basis of the topological theory of interfacial defects. One example is shown in Fig. 4a, which is a higher magnification cross-sectional HRTEM image obtained from a typical region of a C_1 facet with the beam direction parallel to the conjugate close-packed directions. An example of a circuit used to deduce the defect character of the

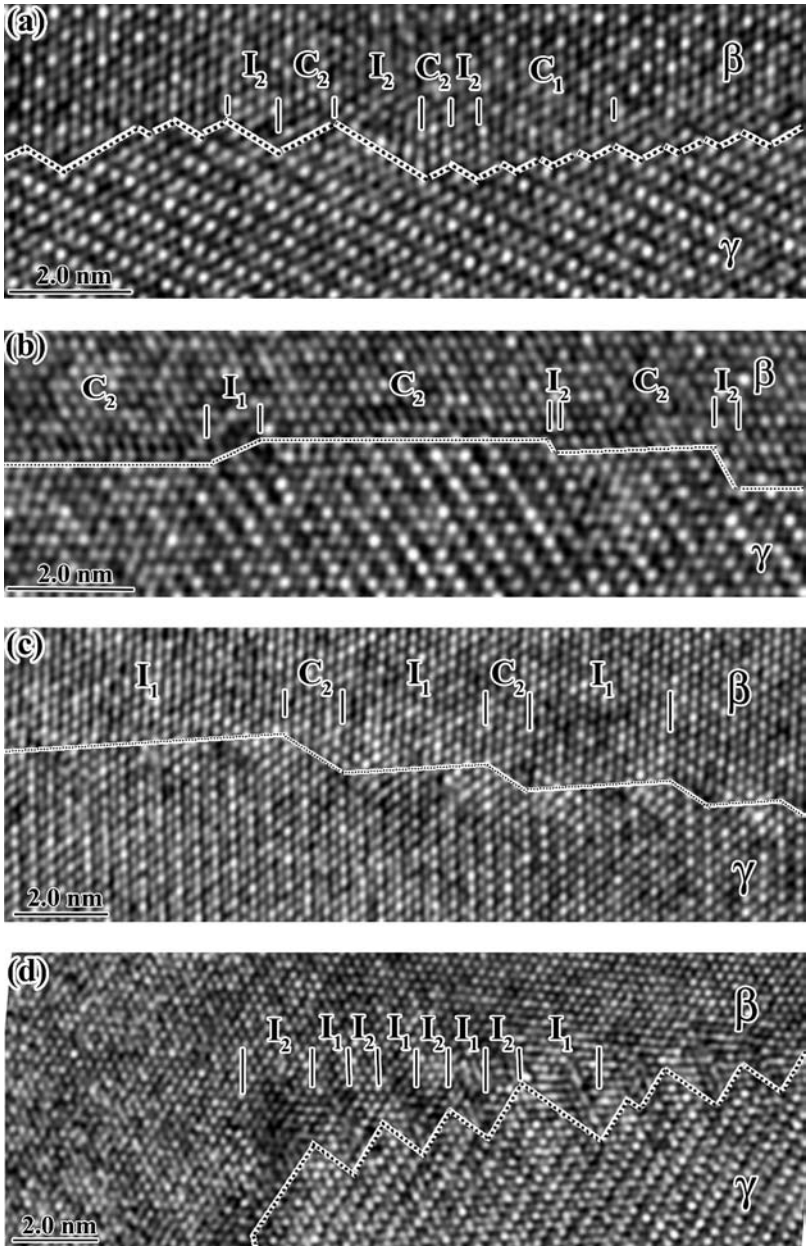

Figure 3 HRTEM images obtained with $\mathbf{B} = [\bar{1}\bar{1}\bar{1}]_\beta * //[\bar{1}10]_\gamma *$ showing: (a) C_2 and I_2 microfacets at a C_1/C_2 facet junction; (b) I_1 and I_2 microfacets interrupting a narrow C_2 facet; (c) I_1 and C_2 microfacets at an I_1/C_2 facet junction; (d) I_1 and I_2 microfacets at an I_2/I_1 facet junction.

steps is shown in this figure. Since the terraces of these facets correspond to the defect-free coherent structure of the C_2 facets, this was chosen as the reference state for the mapping. Fig. 4b is the corresponding dichromatic pattern constructed at the K-S OR so that $[1\bar{1}0]_\gamma //[111]_\beta$, $[111]_\gamma //[10\bar{1}]_\beta$, $[11\bar{2}]_\gamma //[1\bar{2}1]_\beta$, with the latter directions being made coherent by applying a small strain to the γ phase. We note that the application of this strain is necessary to produce a commensurate reference state otherwise, as noted by Medlin *et al*. [8], the value of the Burgers vector obtained from the circuit mapping will depend upon the size of the circuit. If we assume for simplicity that both phases are disordered, β being bcc with $a_\beta = 0.318$ nm, and γ being fcc with $a_\gamma = 0.403$ nm (the mean of the a and c parameters for this $L1_0$ phase) then the coherency strain required along $[11\bar{2}]_\gamma //[1\bar{2}1]_\beta$ is a dilation of the γ phase by 6.3%. For these values, the co-ordinate transformation matrix corresponding to the reference state is:

$$\mathbf{P}_{\beta\rightarrow\gamma} = \begin{bmatrix} 0.7826 & 0.0758 & 0.1267 \\ 0.1259 & -0.5809 & -0.5300 \\ 0.0701 & 0.5050 & -0.5753 \end{bmatrix}$$

Circuit maps were constructed around several examples of steps such as those shown in Fig. 4a and in each case the

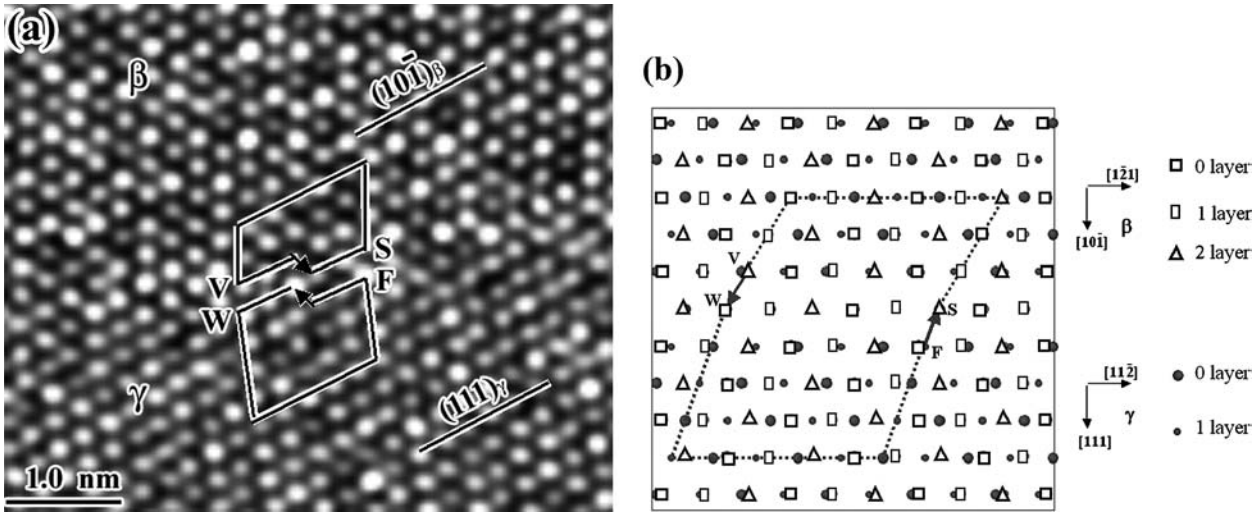

Figure 4 Structure of the C_1 facets: (a) HRTEM image (obtained with $\mathbf{B} = [\bar{1}\bar{1}\bar{1}]_\beta * // [\bar{1}10]_\gamma *$) with a Burgers circuit superimposed; (b) Dichromatic pattern projected along $[\bar{1}\bar{1}\bar{1}]_\beta$and $[\bar{1}10]_\gamma$ showing the reference structure at the K-S OR with the close-packed planes $(10\bar{1})_\beta$ and $(111)_\gamma$ parallel.

value of the Burgers vector, **b**, obtained for these features was:

$$\mathbf{b} = [-0.210, 0.118, 0.070]\gamma,$$

Defects with finite Burgers vectors and step heights are described formally as disconnections [5, 6]. The effects of the disconnections in the C_1 facet can be seem most clearly by resolving their Burgers vectors into projected components $\mathbf{b}_{//}$ and $\mathbf{b}_\perp$, parallel and perpendicular to the terrace, respectively. The values of these components are $\mathbf{b}_{//} = 0.039[11\bar{2}]_\gamma$ and $\mathbf{b}_\perp = 0.007[\bar{1}\bar{1}\bar{1}]_\gamma$, which have magnitudes of 0.041 nm and 0.005 nm, respectively. The effect of an array of disconnections with spacing d and Burgers vector components $\mathbf{b}_{//}$ of the same sign is to produce a strain $\varepsilon = \mathbf{b}_{//}$ / d parallel to the interface. For the measured values of d (0.7 nm) and $\mathbf{b}_{//}$ (0.041 nm), $\varepsilon = 5.9\%$. Both the sense and magnitude of this strain are consistent with that used to produce the reference state shown in Fig. 4b, i.e. the defect spacing corresponds to that required to give a coherent interface. In a similar manner we can see the effects of the Burgers vector components $\mathbf{b}_\perp$, upon the orientation by treating the interface as a low angle tilt boundary for which the rigid body rotation, $\theta = \mathbf{b}_\perp/\mathrm{d}$. For the measured values of d (0.7 nm) and $\mathbf{b}_\perp$ (0.005 nm), $\theta = 0.41^\circ$, which is very close in both sense and magnitude to the deviation between the measured OR and the K-S OR for the reference state.

3.4. Structure and defect content of the I_1 facets

A similar analysis was performed upon structure of the I_1 facets and a cross-sectional HRTEM image of a typical region is shown in Fig. 5a. The habit plane of the facet is exactly $(110)_\gamma/(2\bar{1}\bar{1})_\beta$ and it appears to be incommensurate, although arrays of defects can still be observed in the interface with a mean spacing of ≈ 1.5 nm. These were analyzed using circuit mapping with the reference state shown in Fig. 5b. This is a dichromatic pattern constructed at the Pitsch OR so that $[1\bar{1}0]_\gamma//[111]_\beta$, $[110]_\gamma//[2\bar{1}\bar{1}]_\beta$, $[00\bar{1}]_\gamma//[0\bar{1}1]_\beta$. Here again, it was necessary to apply a strain to the γ phase in the latter direction to produce a coherent structure so that consistent results could be obtained for circuit mapping. In this case, however, the magnitude of the strain is larger (11.3%) and its physical significance is more questionable given that the observed structure is incommensurate. Using this strain and making the same approximations for the lattice parameters as before, the co-ordinate transformation matrix corresponding to the reference state is:

$$\mathbf{P}_{\beta\to\gamma} = \begin{bmatrix} 0.7800 & 0.0095 & 0.0095 \\ 0.1338 & -0.5515 & -0.5515 \\ 0 & 0.4956 & -0.4956 \end{bmatrix}$$

Circuit maps were constructed around several examples of the defects such as those shown in Fig. 5a and in each case, the value of **b** obtained for these features was either $0.5[0\bar{1}1]_\gamma$ or $0.5[\bar{1}01]_\gamma$. Clearly, these values of **b** correspond to those for perfect crystal dislocations in the fcc lattice (although both would correspond to superpartial dislocations when the ordering is taken into account). The projected components of these Burgers vectors are $\mathbf{b}_{//} = 0.5[001]_\gamma$ and $\mathbf{b}_\perp = 0.25[110]_\gamma$ which have magnitudes of 0.202 nm and 0.142 nm, respectively. The effect of the components $\mathbf{b}_{//}$ is to produce a strain $\varepsilon \approx 11.3\%$ as expected, since this is what would be required to relax the strain imposed in creating the coherent reference state.

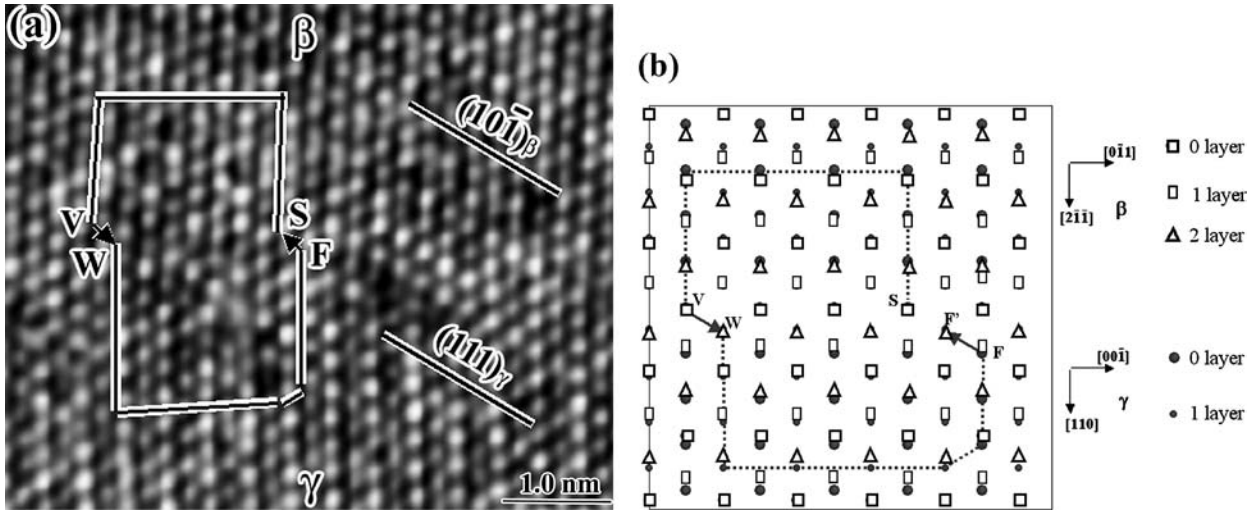

Figure 5 Structure of the I_1 facets: (a) HRTEM image (obtained with $\mathbf{B} = [\bar{1}\bar{1}\bar{1}]_\beta * // [\bar{1}10]_\gamma *$) with a Burgers circuit superimposed; (b) Dichromatic pattern projected along $[\bar{1}\bar{1}\bar{1}]_\beta$ and $[\bar{1}10]_\gamma$ showing the reference structure at the Pitsch OR with $[0\bar{1}1]_\beta$ parallel to $[00\bar{1}]_\gamma$.

We note that the choice of a different coherent reference state involving a larger strain would give Burgers vectors with larger values of $\mathbf{b}_{//}$, but here again these would balance the strain imposed to create the reference state. The values of $\mathbf{b}_\perp$ are, however, independent of the reference state and the rigid body rotation θ introduced by the array of defects is $\approx$ 5.44°. This is consistent with both the magnitude and sense of the defect content required to accommodate the angular deviation between the measured OR and the Pitsch OR for the reference state.

4. Discussion

The γ precipitates studied in this work will have little impact upon the mechanical behavior of the alloy because they are found only within the grain boundary β phase and thus their total volume fraction is very low. They do, however, constitute a very interesting case study for interfacial structure and defect content. The precipitates adopt an acicular morphology with a rather irregular cross-section. More detailed examination revealed that this morphology comprises four distinct types of facets: two exhibiting coherent atomic structures (C_1 and C_2) and the other two exhibiting one-dimensionally incoherent atomic structures (I_1 and I_2), although the coherence parallel to the major axis of the precipitate will be the same in each case.

The C_1 and I_1 facets are much larger than the C_2 and I_2 facets indicating that the former types are much lower energy configurations. This is an interesting result since the C_1 facets exhibit a corrugated step/terrace atomic structure, which appears to correspond to an intimate combination of the C_2 and I_2 facets. In section 3.3 it has been shown that a more accurate representation of the atomic structure for the C_1 facets is one in which the terraces correspond to regions with the C_2 facet structure and the risers of the steps lie parallel to the habit plane of the I_2 facets but are *coherent*. As such, these steps correspond to interfacial disconnections. An analysis of the defect content in the interface due to these disconnections has shown that the Burgers vector components parallel to the terrace plane have the appropriate sign and magnitude to accommodate the coherency strains on the terraces. Thus, the C_1 facets exhibit a low-energy relaxed structure, which would account for the relatively large areas of these facets and the constant spacing of the steps. We note that this is consistent with the results of atomistic simulations on other fcc/bcc systems (e.g. [9]), which have shown such interface configurations to have particularly low energies. To our knowledge, no such simulations have been performed for the incoherent I_1 facet structure, but since the I_1 facets are of a similar size to the C_1 facets we infer that they have similar low energies.

One of the most remarkable aspects of this system is that the two major facets exhibit low energy structures at *different* reference orientations. The coherent C_2 structure formed on the terraces of the C_1 facets arises at exactly the K-S OR. The array of disconnections that accommodates the coherency strains also introduces a rigid body rotation of $\approx 0.5°$ about the conjugate close-packed directions away from the Pitsch OR: this gives the OR for the relaxed reference state which corresponds to the orientation observed experimentally. The low-energy structure for the I_1 facets arises at the Pitsch OR. This difference in OR must be accommodated by compatibility defects if long-range strains are to be avoided [10]. There are no additional defects in the C_1 facets to fulfill this role but there are suitable crystal dislocations in the I_1 facets. By employing a low-angle grain boundary model we have shown that the Burgers vector components perpendicular

to the interface would account well for the angular incompatibility between the Pitsch OR and the orientation observed experimentally.

It is interesting to contrast these observations with our recent data obtained from a duplex stainless steel [4, 10]. In this latter system the fcc γ precipitates also exhibited acicular morphologies and were bounded by major facets which closely resemble the C_1 and I_1 facets in the present system. The OR for the γ precipitates in the stainless steel varied somewhat from particle-to-particle and the mean OR was slightly different from that in the titanium aluminide alloy. It was proposed that when the γ precipitates nucleate it may be energetically favorable for the orientation incompatibility to be accommodated by disclinations at the facet junctions since the dislocation mechanisms that are required to annihilate their strain fields are not able to operate [11]. We note, however, that the energies of disclination multipoles vary with a^2, where a is the disclination separation (e.g. [12]). Therefore one would expect tilt walls of crystal dislocations to be introduced relieve the long-range displacement fields of the disclinations as the particles coarsen. For the γ precipitates in the stainless steel, the crystal dislocations were found in both major facets, giving a precipitate orientation intermediate between the ORs for the relaxed coherent structure and the incoherent structure. Moreover, small differences in the partitioning of these defects between the two facets from particle-to-particle gave rise to the observed variation in particle orientation.

For the γ precipitates in the titanium aluminide alloy, however, the crystal dislocations were found in the I_1 facets only giving rise to a singular OR corresponding to that for the relaxed structure of the C_1 facets. By analogy with the stainless steel case, it is tempting to speculate that these precipitates may also form initially as nanoscale rods bound by C_1 and I_1 facets with disclinations at the facet junctions. If so then as the rods coarsen, the elastic energy of the disclination quadrupole will rise until the point at which it is energetically favorable to introduce crystal dislocations as compatibility defects. There are two main ways in which this could occur; by shearing within the precipitate or by climb along the interface from the disclination cores. The former mechanism seems highly unlikely since one would expect equal activity on equivalent glide planes: this would give compatibility defects in both the C_1 and I_1 facets for this precipitate geometry. Moreover, since the Burgers vectors determined for the compatibility defects are those of superpartial dislocations, one would expect to observe trailing anti-phase boundaries on the glide planes but no such planar defects were observed in any of the particles. As such, it seems likely that the compatibility defects are introduced by climb from the disclination core during coarsening. The observation of these defects in the I_1 facets but not the C_1 facets is consistent with this mechanism since one would expect the associated diffusional processes to be much faster in the I_1 facets than in the C_1 facets.

5. Conclusions

The morphology, interfacial structure and defect content for γ precipitates in the retained β phase of a Ti-44Al-4Nb-4Zr alloy have been studied by TEM and HRTEM. These observations have enabled us to draw the following conclusions:

- The precipitates exhibit a fixed orientation, which is $\approx 0.5^\circ$ away from the K-S OR: this deviation corresponds to a rotation about the conjugate close-packed directions away from the Pitsch OR.
- The precipitates exhibit a characteristic acicular morphology with their major axes parallel to the conjugate close-packed directions. The cross-sections of these precipitates are rather irregular and are bounded by two coherent facets and two incoherent facets.
- The major coherent C_1 facets exhibit a 'step-terrace' atomic structure. The steps correspond to interfacial disconnections whose defect character accommodates the coherency strains on the terraces and gives the relaxed facet structure the orientation observed experimentally.
- The major incoherent I_1 facets exhibit a planar 1–D incommensurate structure corresponding to the Pitsch OR. The orientational incompatibility between these and the misfit-relieved C_1 facets is accommodated by additional dislocation content in the I_1 facets.
- The observations indicate that the γ precipitates nucleate as dislocation-free particles with disclinations at the facet junctions. As the precipitates coarsen, the strain fields of these disclinations are relieved by dislocations, which are generated at the facet junctions and then climb along the I_1 facets. The fixed OR is due to the climb being much more rapid along the I_1 facets than along the C_1-facets.

Acknowledgments

The authors would like to thank Dr. T.T. Cheng and Prof. R.C. Pond for helpful discussions. This work was supported by the National Science Foundation under Grant # DMR-0072721.

References

1. H. M. FLOWER and J. CHRISTODOULOU, *Mater. Sci. Tech.* **15** (1999) 45.
2. T. T. CHENG, M. R. WILLIS and I. P. JONES, *Intermetallics.* **7** (1999) 89.
3. T. T. CHENG and M. H. LORETTO, *Acta Mater.***46** (1998) 4801.
4. H. S. JIAO, M. AINDOW and R. C. POND, *Philos. Mag.* **83** (2003) 1867.

5. R. C. POND, "Dislocations in Solids" vol.8, edited by F. R. N. NABARRO, North Holland, Amsterdam, 1989 pp. 1–66.
6. R. C. POND and J. P. HIRTH, *Solid State Physics*, **47** (1994) 288.
7. R. C. POND, *Interface Science*, **2** (1995) 299.
8. D. L. MEDLIN, D. COHEN and R. C. POND, *Philos. Mag. Lett.* **83** (2003) 223.
9. J. K. CHEN, D. FARKAS and W. T. REYNOLDS, *Acta Mater.* **45** (1997) 4415.
10. R. C. POND, H. JIAO, L. C. ZHANG and M. AINDOW, *Metall. Mater. Trans.* A, 2006 (in press).
11. G. P. DIMITRAKOPULOS, PH. KOMNINOU, TH. KARAKOSTAS and R. C. POND, *Interface Science*. **7** (1999) 217.
12. A. E. ROMANOV and V. I. VLADIMIROV, "Dislocations in Solids" vol. 9, edited by F. R. N. NABARRO, North Holland, Amsterdam, 1992 pp. 191–402.